



New spectrum ratio properties and features for shadow detection



Jiandong Tian^{a,*}, Xiaojun Qi^c, Liangqiong Qu^{a,b}, Yandong Tang^a

^a State Key Laboratory of Robotics, Shenyang Institute of Automation, Chinese Academy of Sciences, Shenyang 110016, Liaoning Province, PR China

^b University of Chinese Academy of Sciences, Beijing 100049, PR China

^c Department of Computer Science, Utah State University, Logan, UT 84322-4205, USA

ARTICLE INFO

Article history:

Received 28 January 2015

Received in revised form

13 July 2015

Accepted 5 September 2015

Available online 23 October 2015

Keywords:

Spectrum ratio properties

Shadow features

Skylight SPD

Daylight SPD

Shadow detection

ABSTRACT

Successfully detecting shadows in still images is challenging yet has wide applications. Shadow properties and features are very important for shadow detection and processing. The aim of this work is to find some new physical properties of shadows and use them as shadow features to design an effective shadow detection method for outdoor color images. We observe that although the spectral power distribution (SPD) of daylight and that of skylight are quite different, in each channel, the spectrum ratio of the point-wise product of daylight SPD with sRGB color matching functions (CMFs) to the point-wise product of skylight SPD with sRGB CMFs roughly approximates a constant. This further leads to that the ratios of linear sRGB pixel values of surfaces illuminated by daylight (in non-shadow regions) to those illuminated by skylight (in shadow regions) equal to a constant in each channel. Following this observation, we calculated the spectrum ratios under various Sun angles and further found out four new shadow properties. With these properties as shadow features, we developed a simple shadow detection method to quickly locate shadows in single still images. In our method, we classify an edge as a shadow or non-shadow edge by verifying whether the pixel values on both sides of the Canny edges satisfy the three shadow verification criteria derived from the shadow properties. Extensive experiments and comparison show that our method outperforms state-of-the-art shadow detection methods.

© 2015 Elsevier Ltd. All rights reserved.

1. Introduction

Shadows are physical phenomena observed in most natural scenes. Recently, shadow detection has attracted a lot of attention in computer vision and pattern recognition communities. Shadows in an image can provide useful information about the scene. For example, they provide cues about the location of the Sun as well as the shape and the geometry of the occluder. Lalonde et al. [1] employed detected shadows to estimate the most likely illumination direction in outdoor scenes. Cao and Hassan [2] employed multiple views of objects and their cast shadows to perform camera calibration. Kawasaki and Furukawa [3] proposed a method to reconstruct 3D scenes using cast shadows and scene geometries. On the other hand, removing shadows in an image significantly aids in a wide range of important computer vision tasks, such as feature extraction, image segmentation, object detection, and object tracking. Based on shadow detection methods, some shadow removal methods (like [4–7]) can be applied to remove the detected shadows. No matter utilizing or removing

shadow, it should be detected first. Therefore, shadow detection is of great practical significance in computer vision and pattern recognition.

For shadow detection on images, a high proportion of shadow detection methods focus on detecting moving shadows [8–14]. Moving shadow detection methods firstly employ the frame difference technique to locate moving objects and their moving shadows. The problem of shadow detection then becomes differentiating the moving objects from the moving shadows. Recently, learning approaches are commonly applied in the shadow detection literature. The representative learning approaches include the Gaussian mixture model [15] for learning the background appearance variations under cast shadow, the unsupervised kernel-based model [16] for estimating the cast shadow direction, and the Support Vector technique for co-training different shadow features [17]. Interested readers may refer to [18,19] for a good review of shadow detection methods in video sequences. However, these successful moving shadow detection methods cannot be applied to detect static shadows in a single image.

Compared with detecting moving shadows, detecting static shadows is a more challenging task. It can be applied in a larger variety of applications and has recently been attracting more attentions in computer vision and pattern recognition. Some static

* Corresponding author. Tel. +86 24 2397 0051; fax: +86 24 2397 0021.

E-mail addresses: tianjd@sia.cn (J. Tian), Xiaojun.Qi@usu.edu (X. Qi), quliangqiong@sia.cn (L. Qu), ytang@sia.cn (Y. Tang).

shadow detection methods require two images to provide complementary information for a more accurate shadow detection. Finlayson et al. [20] employed a chromogenic camera to take two pictures of a scene to detect shadows. Iwama et al. [21] proposed a calibrated binocular camera-based method to segment shadows. As a special application of detecting shadow in single images, some literatures [22–24] focus on detecting shadows in aerial images. Very recently, learning approaches have been extended from moving shadow detection to static shadow detection. Lalonde et al. [25] proposed a conditional random field learning approach to detect ground shadows in consumer-grade photographs. Zhu et al. [26] combined boosted decision tree and conditional random field learning to detect shadows in monochromatic images. Guo et al. [27] trained their classifier using SVM with the RBF kernel to detect shadows for a single image. Panagopoulos et al. [28] employed the Fisher distribution learning method to model shadows with 3D geometry information as prior knowledge. The performance of these learning-based methods often depends on the training sets. In other words, learning on different training sets may lead to different shadow detection results. Furthermore, these learning-based methods may be time-consuming since they often need to extract complex statistical features, e.g., texture and histogram, to feed into the classifier for detecting shadows. As a result, they may not be applicable in real-time applications.

Despite these extensive studies, robust static shadow detection remains a difficult problem. To a large extent, it is due to the lack of robust shadow features. The most straightforward feature of a shadow is that it darkens the surface it casts on. This feature is adopted by some methods directly [23] or indirectly [12]. Other features like histograms [29], texture [30], color ratio [31], and gradient [32] are also frequently adopted. These features may not be robust enough in some applications. For example, shadowed regions are often dark, with less texture and little gradient, but some non-shadowed regions may also have similar characteristics. Therefore, new shadow properties and features are important to perform shadow detection and processing.

As a nature phenomenon, a shadow has physical properties that should be adopted in shadow detection. As illustrated in Fig. 1, humans may identify a shadow by exploring the contrast near edges. Without contrast, it is difficult to determine whether the color checker is in the shadow or not. Therefore, the contrast between the shadow and its background should be used to perform the shadow detection task. In our previous work [33], we proposed the tricolor attenuation model that describes the attenuation relationship between a shadow and its non-shadow background in three color channels. In our follow-up work [34], we further deduced a linear model that describes the pixel values of surfaces in a shadow region and a non-shadow region have a linear relationship. The aim of this work is to find additional new physical properties of shadows by analyzing the sRGB color matching functions (CMFs) and spectral power distribution (SPD) of illumination, and then take these shadow properties as features to design a novel and effective shadow detection method. The contributions of this paper include:

- We observe that in each color channel the point-wise product of daylight SPD with CMFs ($H=R, G, B$) roughly approximates to the point-wise product of skylight SPD with CMFs ($H=R, G, B$) multiplying a constant (we name it as spectrum ratio). We further show that the ratio of pixel values of a surface illuminated by daylight vs. those by skylight equals to the constant, which is independent of surface reflectance and holds true in each of the three color channels.
- Based on the calculated spectrum ratios under various representative Sun angles, we found out four new shadow properties which represent physical characteristics of shadows.
- Following the four new shadow properties, we derive three verification criteria and then propose an effective shadow detection method which can quickly locate shadows.

The rest of the paper is organized as follows. In Section 2, we describe the deduced spectrum ratio properties of shadows. In Section 3, we describe the shadow detection method. In Section 4,

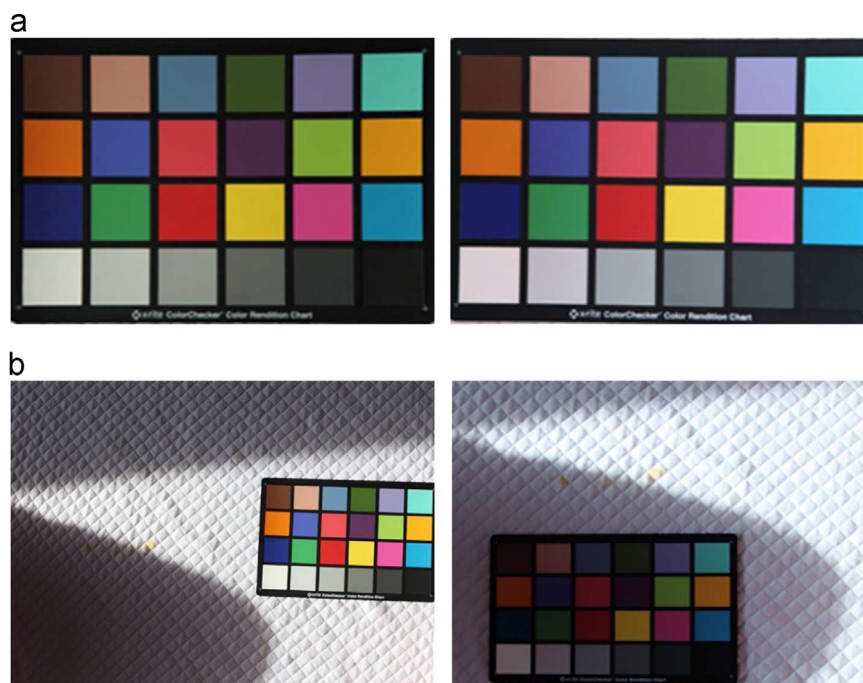


Fig. 1. Illustration of non-obvious and obvious shadows. It is much easier for us to identify shadows by exploring the contrast near edges. The two checkerboards shown in (a) were captured under identical imaging environment with the two pictures shown in (b).

we show and analyze the experimental results. We end this paper with a brief discussion and conclusion in Section 5.

2. Spectrum ratio properties of shadows

2.1. Spectrum ratio

Given the SPD of illumination $E(\lambda)$, objects reflectance $S(\lambda)$, and sRGB CMFs $Q(\lambda)$, the linear sRGB tristimulus values for visible light whose spectrum ranges from 400 nm to 700 nm are computed by

$$\mathcal{F}_H^L = \eta \cdot w_H \cdot \int_{400}^{700} E(\lambda)S(\lambda)Q_H(\lambda) d\lambda, \quad (1)$$

where

- The superscript L denotes non-Gamma corrected linear pixel values;
- The subscript H denotes the red, green, and blue channel when replaced with $R, G,$ and $B,$ respectively;
- w_H represents the white balance factor, in the case of $S(\lambda) = 1,$ for the red, green, and blue channel, which simultaneously satisfies the following two conditions [35]:

$$w_G = 1 \quad \text{and} \quad w_R \cdot \mathcal{F}_R^L = w_G \cdot \mathcal{F}_G^L = w_B \cdot \mathcal{F}_B^L \quad (2)$$

- η is a factor to approximate the camera exposure and is defined as follows:

$$\eta = \frac{100}{\int_{400}^{700} E(\lambda) \cdot Q_G(\lambda) d\lambda} \quad (3)$$

Gamma correction can be applied on Eq. (1) to convert the linear sRGB values to sRGB values by

$$\mathcal{F}_H = 255 \cdot \left[1.055 \cdot \left(\frac{\mathcal{F}_H^L}{100} \right)^{(1/2.4)} - 0.055 \right] \quad (4)$$

In order to seek shadow characteristics that are independent of surface reflectance, we investigate the point-wise product of the outdoor illumination and sRGB CMFs since illumination and camera spectral responses have much less randomness than reflectance. In the following, we will use the SPD of Sun angle at 60° (Fig. 2) as an example. Fig. 3 shows the results by point-wisely multiplying the SPD of daylight and skylight with the CMFs for the red, green, and blue channel. We observe that though the SPD of daylight and skylight are quite different, in each color channel, the point-wise product of daylight SPD with CMFs ($H = R, G, B$) roughly approximates to the point-wise product of skylight SPD with CMFs

($H = R, G, B$) multiplying a constant. That is,

$$E_{day}(\lambda) \cdot Q_H(\lambda) \approx K_H \cdot E_{sky}(\lambda) \cdot Q_H(\lambda) \quad (5)$$

where K_H (we name it as spectrum ratio) is a constant independent of wavelength and is different in $H = R, G, B$ channel. It is equivalent to find an optimal K_H that minimizes the difference between the point-wise product results of the SPD of daylight with the CMFs and the scaled point-wise product results of the SPD of skylight with the CMFs. This optimization problem can be formulated as follows:

$$\arg \min_{K_H} \sum_{\lambda=400}^{700} |E_{day}(\lambda) \cdot Q_H(\lambda) - K_H \cdot E_{sky}(\lambda) \cdot Q_H(\lambda)| \quad (6)$$

We apply the simple exhaustive search method to solve this optimization problem. We set the sampling step size of λ in Eq. (6) as 10 nm and set the step size of K_H as 0.01. The derived three constants (6.79, 5.92, and 4.24 for red, green, and blue channels, respectively) are used to generate the three plots in Fig. 3.

In the following, we will show that in each channel, the linear sRGB pixel values of a surface illuminated by daylight are proportional to those of the same surface illuminated by skylight, and the proportional coefficients equal to spectrum ratios K_H .

We replace $E(\lambda)$ in Eq. (1) with $E_{sky}(\lambda)$ to model the linear sRGB tristimulus values for visible light on a surface in a shadow area by

$$f_H^L = \eta \cdot w_H \cdot \int_{400}^{700} E_{sky}(\lambda)S(\lambda)Q_H(\lambda) d\lambda \quad (7)$$

Similarly, we replace $E(\lambda)$ in Eq. (1) with $E_{day}(\lambda)$ to model the linear sRGB tristimulus values for visible light on the same surface in a non-shadow area by

$$F_H^L = \eta \cdot w_H \cdot \int_{400}^{700} E_{day}(\lambda)S(\lambda)Q_H(\lambda) d\lambda \quad (8)$$

If we divide Eq. (8) by Eq. (7) and combine with Eq. (5), we have,

$$\frac{F_H^L}{f_H^L} = \frac{\eta \cdot w_H \cdot \int_{400}^{700} E_{day}(\lambda)S(\lambda)Q_H(\lambda) d\lambda}{\eta \cdot w_H \cdot \int_{400}^{700} E_{sky}(\lambda)S(\lambda)Q_H(\lambda) d\lambda} \approx K_H \quad (9)$$

From Eq. (9), we can find that the linear sRGB tristimulus values of a surface illuminated by daylight are proportional to those of the same surface illuminated by skylight in each of the three color channels. Furthermore, the proportional coefficients are independent of reflectance and approximately equal to the spectrum ratios determined by Eq. (6). Since most consumer photographic image formats such as JPEG, BMP and TIF are encoded in the sRGB color space and are Gamma corrected, it is necessary to investigate how to calculate K_H from Gamma corrected sRGB values. From Eq. (4),

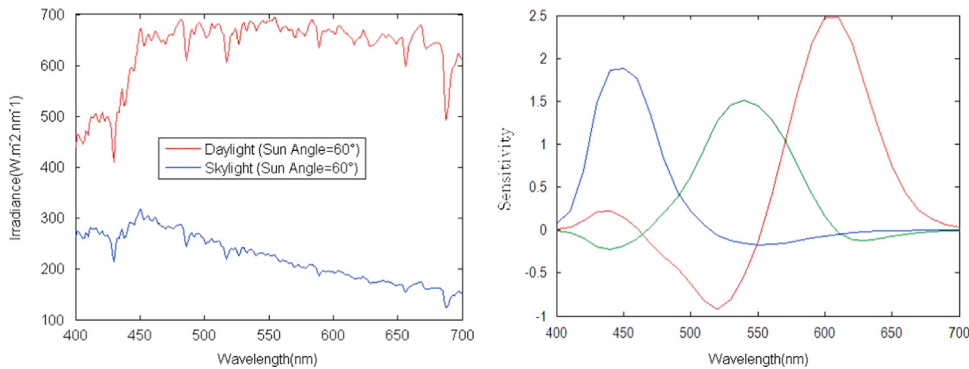


Fig. 2. SPD of daylight and skylight at Sun angle of 60° (left) and sRGB CMFs (right).

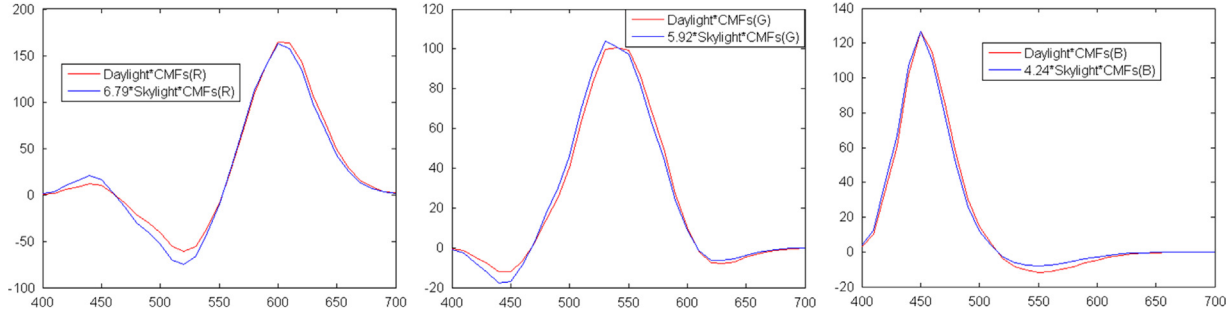


Fig. 3. The point-wise products of daylight SPD with CMFs can be well approximated by those of skylight SPD with CMFs multiplying a constant in each channel. The constants are derived by Eq. (6).

Table 1

Spectrum ratios and their differences at representative Sun angles.

Spectrum ratios	20°	30°	40°	50°	60°	70°	80°
K_R	12.11	10.26	9.49	8.59	6.79	4.79	3.18
K_G	10.40	9.19	8.52	7.40	5.92	4.25	2.86
K_B	8.10	7.28	7.19	5.94	4.24	3.58	2.53
$K_R - K_G$	1.71	1.07	0.97	1.19	0.87	0.54	0.32
$K_G - K_B$	2.30	1.91	1.33	1.46	1.68	0.67	0.33

we have,

$$\begin{cases} F_H = 39.5 \cdot F_H^{L(1/2.4)} - 14 \\ f_H = 39.5 \cdot f_H^{L(1/2.4)} - 14 \end{cases} \quad (10)$$

Then we have,

$$\left(\frac{F_H^L}{f_H^L}\right)^{(1/2.4)} = \frac{F_H + 14}{f_H + 14} \quad (11)$$

Based on Eq. (9), we can simplify Eq. (11) to the following:

$$K_H = \left(\frac{F_H + 14}{f_H + 14}\right)^{2.4} \quad (12)$$

Equation (12) shows spectrum ratios can be directly calculated from the Gamma corrected sRGB pixel values by: $K_H = \left(\frac{F_H + 14}{f_H + 14}\right)^{2.4}$. Certainly, we can also convert the Gamma corrected sRGB values to linearized values by inverse Gamma correction and calculate K_H by $K_H = F_H^L / f_H^L$. Both methods are quite unsophisticated. More details about the derivation and verification can be found in our previous work [34]. The advantage of taking the spectrum ratios as physical properties of shadows is that they are independent of wavelength and reflectance.

2.2. New shadow properties

Similar to calculating K_H in 60°, we can further calculate K_H in other representative Sun angles ranging from 20° to 80°. We measured SPDs of daylight and skylight at representative Sun angles by an Avantes USB 2.0 spectrometer for one year. In meteorology, there are SPD calculation methods based on analyzing the transmittance functions of absorption and scattering along the path solar radiation through the atmosphere. The two representative spectral models include SMARTS2 [36] and MODTRAN [37]. However, they are too complex to use because there are many parameters to be determined and unfortunately most of these meteorological parameters are not readily available for computer vision applications. Therefore, we measured these SPDs of daylight and skylight rather than modeled them for the K_H calculations. We measured them one or two times each week for one year at different times (Sun angle) and under different

weather conditions. To eliminate the influence of noise and little errors of the measurements, we used mean values of the measurements for the K_H calculation. For most situations that shadow often takes place (e.g., clear weather, little overcast, and big clouds that do not cover the Sun), SPDs of daylight and skylight are relatively stable. They follow a normal distribution as Fig. 2 shows under the same Sun angles. But sometimes, their amplitude varies noticeably; fortunately, the variation in amplitude does not affect the K_H according to Eq. (1). The value of K_H for the Sun angle less than 20° or greater than 80° is not computed since in our and nearby cities, we can only observe Sun angles between 20° and 80°. We used these measured SPDs only to find general rules of K_H , our proposed shadow features are not sensitive to small SPDs variation caused by factors such as time, location, and seasons, since our shadow features and detection methods do not rely on the exact values of K_H . Table 1 lists the spectrum ratios of daylight and skylight for Sun angles from 20° to 80°. To facilitate future discussion, we also list the difference between K_R and K_G and the difference between K_G and K_B for each Sun angle. Table 1 clearly shows the four following new physical shadow properties:

Property 1. The values of K_H decrease as Sun angle increases.

Property 2. The values of K_H ($H = R, G, B$) satisfy $K_R > K_G > K_B$.

Property 3. The differences between K_H ($K_R - K_G$ and $K_G - K_B$) are not very small, and these differences normally decrease as the Sun angle increases. The differences between K_H satisfy $K_R - K_G < K_G - K_B$.

Property 4. The value of K_H at any angle is less than twice of the value of K_H at the next angle, which is 10° larger than the current investigated angle. That is, $K_H^x < 2K_H^{x+10}$, where K_H^x is the value of the K_H at the angle of x .

These referenced shadow properties will be utilized to generate the three shadow verification criteria in our proposed shadow detection algorithm.

3. Shadow detection algorithm

Based on the four new physical shadow properties, we propose a novel shadow detection algorithm for an outdoor color image. Our shadow detection algorithm consists of three steps: multi-threshold edge extraction, K_H calculation, and shadow edge classification. The multi-threshold edge extraction step functions as the preprocessing step, which effectively breaks the connection between shadow edges and object edges. The K_H calculation step employs the dilated regions along the detected edges to compute the values of K_H . The shadow edge classification step employs the three criteria derived from the new shadow properties to classify each edge as shadow edge or non-shadow edge (e.g., object edge). In the following, we explain each of the three steps in detail.

3.1. Multi-threshold edge extraction

We employ the Canny edge detector to extract edges from an image due to its superior performance in extracting thin edges and its robustness to noises. We should avoid long edges since the shadow edge and the object edge may be connected together, which will affect the shadow verification step. To this end, we adopt the multiple thresholds ($T=0.9, 0.8, \dots$, and 0.2) when we employ the Canny edge detector and use the subtraction of Canny results with two adjacent thresholds as the edge images.

3.2. K_H calculation

From Eq. (12), we compute K_H by

$$K_H = \left(\frac{F_H + 14}{\bar{f}_H + 14} \right)^{2.4} \quad (13)$$

where F_H and \bar{f}_H denote the Gamma corrected pixel values of the non-shadow and shadow counterparts, respectively. To overcome noise and obtain fast computing, for each edge, we calculate the mean pixel values on its both sides in each channel to determine the spectrum ratios.

Proposition 1. *The ‘mean’ operation does not change the spectrum ratios computed from the shadow and non-shadow paired pixel elements within the area covered by the mean filter.*

Proof. We rewrite Eq. (13) as follows:

$$F_H + 14 = K_H^{1/2.4} (\bar{f}_H + 14) \quad (14)$$

Suppose we have n shadow and non-shadow counterparts on two sides of an edge, we have,

$$\sum_{i=1}^n F_H^i + 14n = K_H^{1/2.4} \left(\sum_{i=1}^n \bar{f}_H^i + 14n \right) \quad (15)$$

Dividing n on both sides, we have

$$\frac{1}{n} \sum_{i=1}^n F_H^i + 14 = K_H^{1/2.4} \left(\frac{1}{n} \sum_{i=1}^n \bar{f}_H^i + 14 \right) \quad (16)$$

It can then be rewritten as follows:

$$\bar{F}_H + 14 = K_H^{1/2.4} (\bar{\bar{f}}_H + 14) \quad (17)$$

Finally we have

$$K_H = \left(\frac{\bar{F}_H + 14}{\bar{\bar{f}}_H + 14} \right)^{2.4} \quad (18)$$

□

Comparing Eqs. (13) and (18), it clearly demonstrates that the averaged pixel values in non-shadow vs. in shadow region has the same spectrum ratios as its individual non-shadow vs. shadow pixels within the region. In other words, the ‘mean’ operation does not change the spectrum ratios. This conclusion also verifies the claim about Eq. (9) that “the spectrum ratios are independent of the wavelength and reflectance”.

For each detected edge, we enlarge the edge regions by applying a binary dilation operation with size of six pixels on both sides. Fig. 4 illustrates the dilated edge regions for the edge, where the blue area represents the shadow region and the red area represents the non-shadow region.

We calculate the average pixel values in each dilated region along the edge in each color channel. We then take the one with the larger average pixel value as the non-shadow side and the smaller one as the shadow side to compute K_H using Eq. (18).

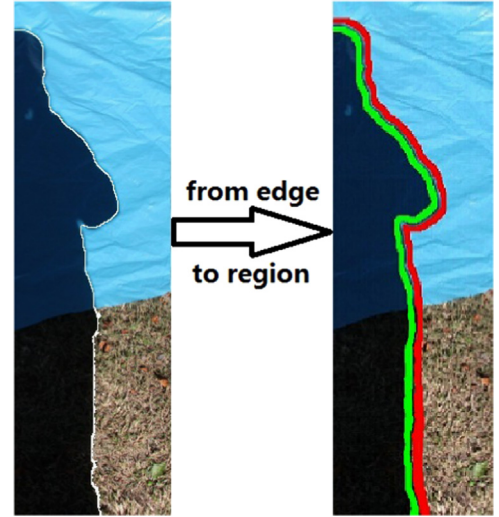


Fig. 4. Illustration of the shadow and non-shadow regions along the Canny edge after applying a binary dilation operation. (For interpretation of the references to color in this figure caption, the reader is referred to the web version of this paper.)

3.3. Shadow edge classification

We finally use the calculated K_H and the aforementioned shadow properties to differentiate shadow edges from object edges. Specifically, we classify the edge as the shadow edge if all of the following three verification criteria are satisfied:

Criterion 1: $\tau_H \cdot K_H^{80} < K_H < \eta_H \cdot K_H^{20}$, where K_H^{80} and K_H^{20} denote K_H at the Sun angles of 80° and 20° , respectively. τ_H and η_H are two predefined tolerance coefficients to decide the lower and upper bounds for the value of K_H . In our system, we adopt these two coefficients since we have to consider all possible values of K_H for Sun angles ranging from 0° to 90° . Table 1 shows that the value of K_H decreases as the Sun angle increases and Property 4 shows the relationship between the values of K_H at two adjacent angles. Based on Property 4, we compute two predefined tolerance coefficients, τ_H and η_H , as follows:

- 1) $\tau_H = 2^{-1}$ since only one angle (i.e., 90°) is greater than 80° when considering the step size of 10° .
- 2) $\eta_H = 2^2$ since two angles (i.e., 10° and 0°) are less than 20° when considering the step size of 10° .

This criterion ensures that a valid range for all values of K_H under different Sun angles is established.

Criterion 2: $K_R > K_G > K_B$, This criterion directly corresponds to the Property 2.

$$\text{Criterion 3: } \begin{cases} K_R - K_G > \varepsilon \wedge K_G - K_B > \varepsilon & \text{if } K_R > K_R^{80} \\ K_R - K_G > \frac{\varepsilon}{2} \wedge K_G - K_B > \frac{\varepsilon}{2} & \text{if } K_R \leq K_R^{80} \end{cases}$$

Parameter ε is the lower bound for the difference between K_R and K_G and the difference between K_G and K_B for Sun angle less than 90° (i.e., $K_R > K_R^{80}$). Since we cannot obtain the differences among three K_H values for Sun angle of 90° in our city and nearby cities, the lower bound for this angle is set to be a half of ε based on the shadow Property 4.

Table 1 shows that $K_R^{80} - K_G^{80}$ is the smallest difference among three K_H values for Sun angles ranging from 20° to 80° . The shadow Property 3 also summarizes that the difference increases as the Sun angle decreases. Therefore, we set ε as

$$\varepsilon = \frac{K_R^{80} - K_G^{80}}{2} \quad (19)$$

Our experiments show that these simple predefined coefficients can achieve good shadow detection performance. Coefficients obtained by other methods (e.g., fitting K_H with different Sun angles, and obtaining two coefficients in each channel) do not offer better performance.

It should be noted that Criterion 2 is a special case of Criterion 3. When $\varepsilon = 0$, Criterion 3 becomes Criterion 2. Here, we list them as two separate criteria due to the following reasons: (1) Criterion 2 does not involve any parameter and has simple expression; (2) Criterion 2 is powerful and robust since it can correctly classify about 85% of non-shadow edges. Thus in some applications that only need coarse shadow detection, Criterion 2 can be separately used for fast detection.

3.4. Algorithm pseudocode and illustration

The detail of our shadow detection algorithm is presented as follows: Algorithm *input*: an outdoor color image Algorithm *output*: shadow edge detected image

```

loop ( $T = 0.9, 0.8, \dots, 0.2$ )
1: Do 'Edge Extraction' Step
   if  $T = 0.9$  then
      $edge \leftarrow Canny(T)$ 
   else
      $edge \leftarrow Canny(T) - Canny(T+0.1)$ 
   endif
2: Do ' $K_H$  Calculation' Step
3: Do 'Edge Classification' Step
End loop

```

Where $Canny(T)$ denotes the results of Canny edge detector on an image with threshold T . The left part in Fig. 5 shows one

original image and its edge images obtained by the multi-threshold edge detector. Two kinds of edges, namely, shadow edges and non-shadow edges are clearly presented in the edge image. The right part in Fig. 5 shows shadow edges satisfying all three criteria and the final shadow detection result. It clearly shows that all non-shadow edges are successfully removed after classification on each edge images. The final result is obtained by adding all shadow edges in different Canny edge images. Matlab code of this paper is available at (http://vision.sia.cn/our_team/JiandongTian/Matlab_codes_of_shadow_detection.zip).

4. Experiments and comparisons

In this section, we compare our proposed shadow detection algorithm with two state-of-the-art shadow detection algorithms [25,27] on various outdoor single color images in terms of shadow detection results, quantitative results, running time, and results on images without shadows. In our experiments, we use images containing shadows with different scenes and reflectance and images that do not contain shadows to test the shadow detection results of the three methods. In Table 2, we summarize the different types of experiments carried out on the paper, the aim of these experiments as well as the types of images used for each type of experiment.

Fig. 6 shows shadow detection results obtained by our method and two state-of-the-art methods [25,27] on seven representative images, which cover a large selection of shadow scenarios. The two images shown in the top two rows contain shadows on surfaces with different reflectance. The image shown in the third row contains noisy shadow. The image shown in the fourth row is a textureless aerial image. The image shown in the fifth row contains shadows on different surfaces such as plastic and grass. The

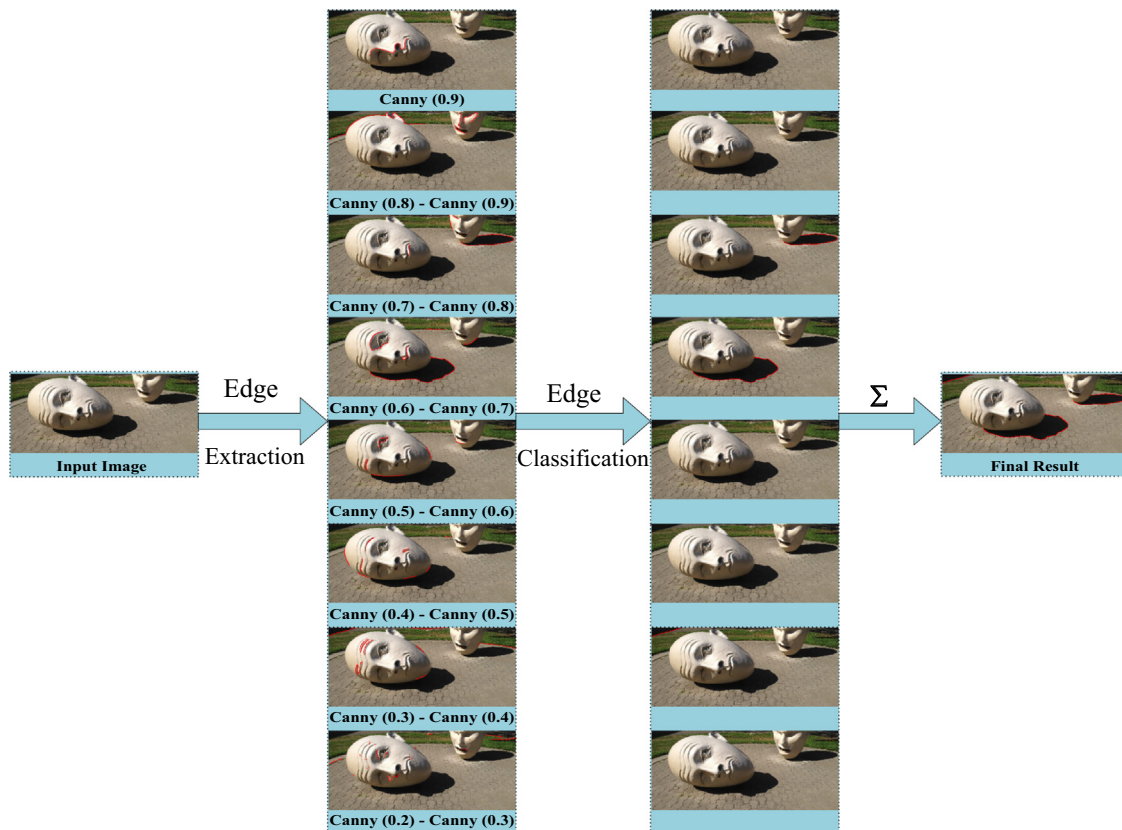


Fig. 5. Shadow edges preserved after shadow classification on Canny edge images.

Table 2

Types of experiments and comparisons carried out on the paper.

Types of experiments	Shadow detection on representative scenarios	Running time	Quantitative results	Detection on images without shadows
Aim of experiments	Compare the three methods on different representative scenarios	Compare the running time of the three methods	Compare quantitative results for the three methods	Compare the three methods on images that do not contain shadows
Images used	Seven representative images that cover a range of scenarios	Also the seven representative images	Four datasets contains 563 real-world images	Two images containing a number of object edges

two images shown in the last two rows contain more complex contents. The shadow detection results of our proposed method, [25] and [27] are presented in the second, third, and fourth columns, respectively. The results and comparisons are summarized as follows:

- 1) For the first two images with different reflectance, our method detects more accurate shadows than Lalonde's method and Guo's method. Both methods miss some shadow edges along the contour of the bicycle and falsely detect some grass and skin as shadow edges.
- 2) For the next three images, our method detects a majority of shadow edges with a few misclassified shadow edges. For example, it detects edges along the curbside in the fourth image as shadows. In comparison, both other methods miss many shadow edges. In detail, Lalonde's method misses some shadow edges of the wheel in the third image and the tree in the fifth image. Guo's method misses most shadows in the third image, mistakenly classifies the edges on the curbside edges in the fourth image as shadow edges, and misses the human body shadow in the fifth image.
- 3) For the last two images, our method successfully detects all the shadow edges with a few misclassified shadow edges. Lalonde's method has false cast shadow detection on the house in the sixth image and on the ground in the last image. Guo's method gives more false positives.

Fig. 6 shows that our proposed shadow detection method achieves better shadow detection results than the other two methods. It should be noted that our method does not require any training and therefore always achieves the same shadow detection results. However, both other methods in comparison sometimes achieve different shadow detection results when employing the learned knowledge from different training images. For example, the learning method [38] can be applied in Lalonde's method to estimate the ground likelihood, which can be combined into the shadow detector to ensure detecting ground shadows. However, incorporating the ground likelihood may not always lead to better shadow detection results. In Fig. 7, we compare the shadow detection results using Lalonde's method without and with ground likelihood, respectively. It shows that Lalonde's method achieves better shadow detection results for the first image when no ground likelihood is incorporated and achieves better shadow detection results for the second image when ground likelihood is incorporated. Similarly, Guo's method produces different shadow detection results when different training sets are used. In Fig. 8, we compare Guo's shadow detection results using Guo's training set and UCF training set. It clearly shows the differences in the shadow detection results by using different training sets. Achieving different results may be a drawback when these methods are applied in real applications, since it is a challenge for a system to automatically identify which result is better. It should be noted that the results of the two compared methods shown in Fig. 6 are the best attained results.

4.1. Running time

Shadow detection usually is a preprocessing step of various practical computer vision tasks. As a result, quick detection is important. We compare the running time of three shadow detection methods, measured in seconds, in Table 3. All experiments were conducted on a computer with Intel (R) Core™ 2 Q8400 2.66 GHz CPU and 2GB RAM memory. The programs were compiled with Matlab R2010b. Table 3 shows that our method is faster than the other two methods.

Guo's method is faster than Lalonde's method in images 1 and 4–7. However, it is slower in images 2 and 3. The average running time on these seven images for our method, Guo's method, and Lalonde's methods is 39.7, 461.0, and 279.7 s respectively. This shows the efficiency of our method.

4.2. Quantitative results

To evaluate whether our method generalizes well to other illumination conditions, we conducted extensive experiments on four datasets including Zhu's dataset [26], Lalonde's dataset [25], Guo's dataset [27], and our dataset. Our dataset contains a variety of images, downloaded from the web or real-captured by a Canon EOS 5D Mark II camera, with scenes that other three datasets do not include. Particularly we carefully captured images under different Sun angles and different weather conditions (include clear sky, little overcast, and big clouds that did not cover the Sun). The four datasets contain 563 real-world images altogether. To the best of our knowledge, we have employed the most extensive images to compare the shadow detection results. We demonstrate some original images with different scenes and our shadow detection results in Fig. 9. Specifically, we test our shadow detection method on images with different reflectance materials (e.g., road, grass, sands, wood, and snow) and different occluders (e.g., shadows of people, building, leaves, and animals). Some images also contain one shadow which covers the areas with different reflectance. Fig. 9 demonstrates that our shadow detection method works well on these different kinds of images. To quantitatively evaluate the effectiveness of our and compared methods, the commonly-used precision, recall, and F-measure are computed.

$$\text{Precision} = \frac{TP}{TP + FN} \quad (20)$$

$$\text{Recall} = \frac{TP}{TP + FP} \quad (21)$$

$$F\text{-measure} = 2 \cdot \frac{\text{Precision} \cdot \text{Recall}}{\text{Precision} + \text{Recall}} \quad (22)$$

Where TP denotes the true shadows that are correctly identified, FN denotes the true shadows that are erroneously classified as non-shadow, and FP denotes the true non-shadow pixels that are erroneously classified as shadows. The higher precision, recall, and F-measure denote better shadow detection results. All these factors are determined by a direct pixel-wise comparison between the ground truth shadow edge map and the predicted

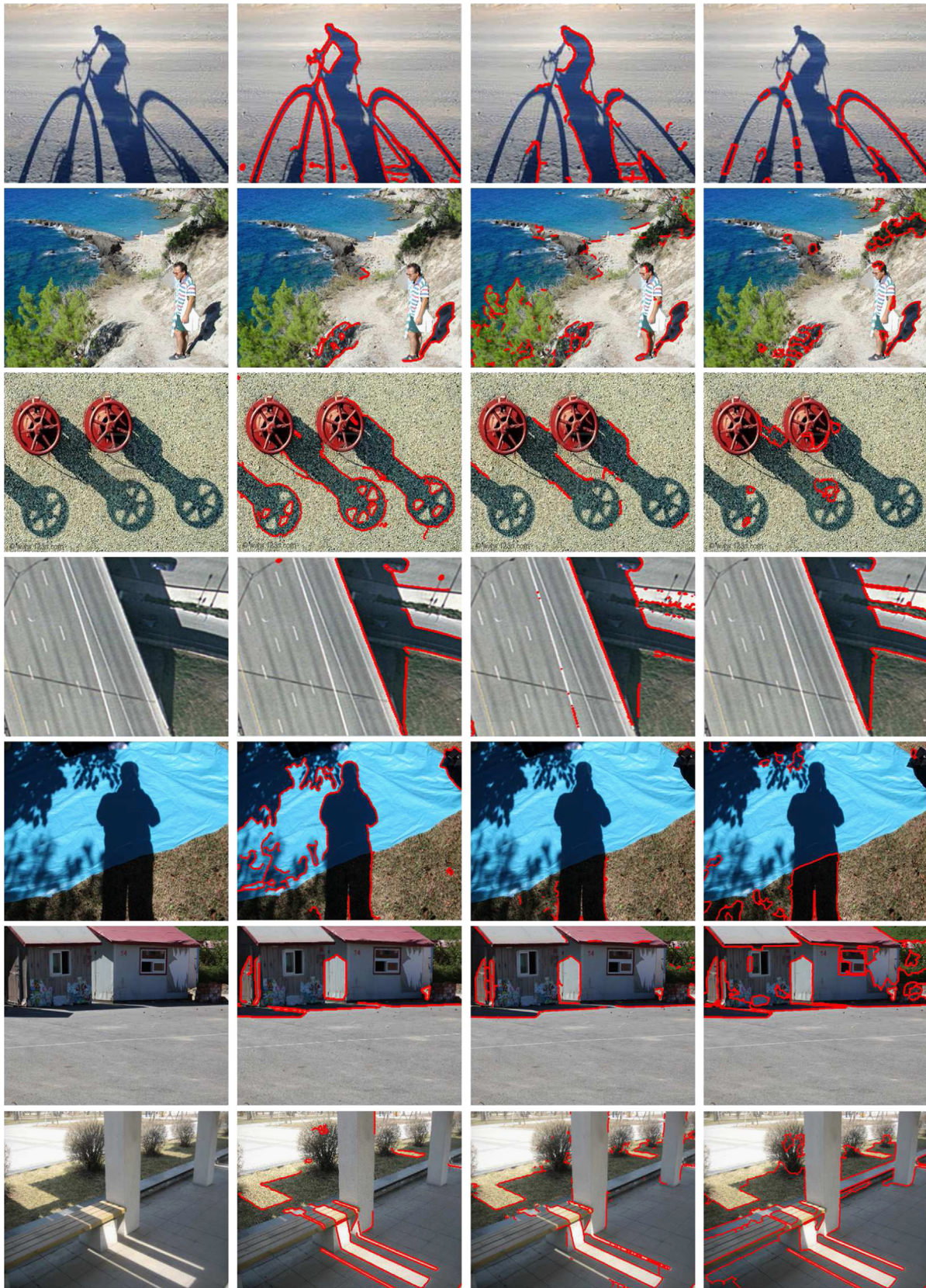


Fig. 6. Comparison with the state-of-the-art methods. 1st column: original images; 2nd column: our results; 3rd column: Lalande's results; 4th column: Guo's results.

shadow edge map. Considering the fact that many of the shadow boundaries are soft, we allow 2 pixel Euclidean distance error between the ground truth and the detected shadow edge maps to

tolerate a slight localization error. Since Guo's method is focused on shadow area detection, we extract its edge maps for a fair result evaluation.

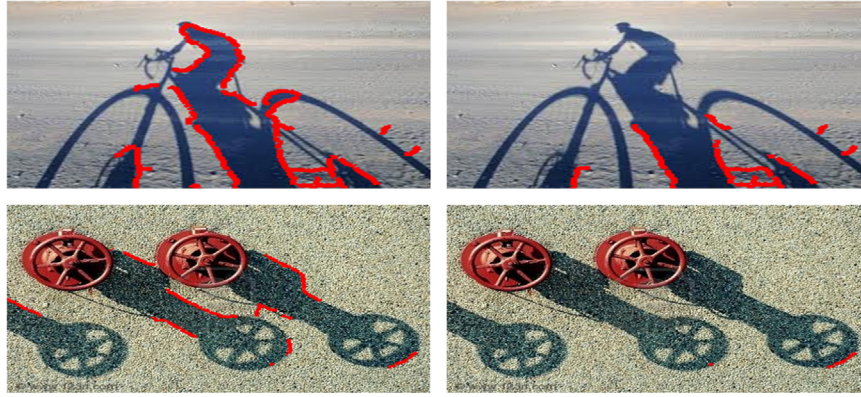


Fig. 7. Different shadow detection results obtained by Lalonde's method without ground likelihood (left) and with ground likelihood (right).

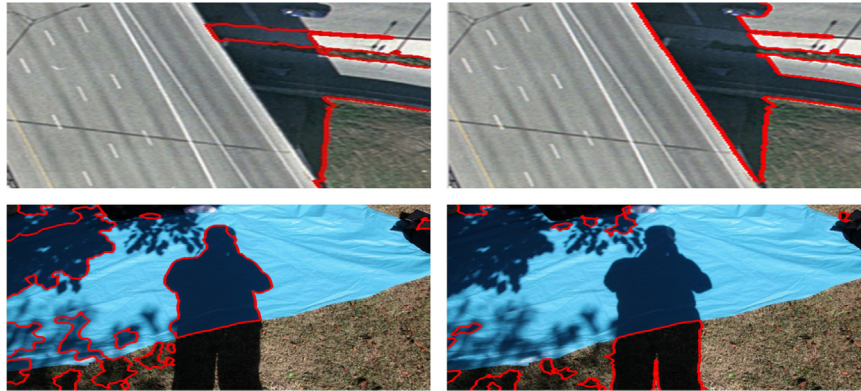


Fig. 8. Different shadow detection results obtained by Guo's method using Guo's training set (left) and using UCF training set (right).

Table 3

Comparison of running time of the three shadow detection methods. Image IDs from 1 to 7 correspond to images in Fig. 6 from top to bottom, respectively.

Method	Images						
	1	2	3	4	5	6	7
Lalonde's	83	267	213	93	391	405	506
Guo's	64	1827	914	44	56	201	121
Ours	10	32	109	12	31	23	61

The experimental results by our results and those by [25,27] on each and the entire dataset is summarized in Table 4. It clearly shows that our method achieves the highest precision, recall, and F-measure on all images, indicating that our method is the most robust, and that our proposed four shadow properties and three shadow verification criteria are effective. Additionally, on each dataset, our method outperforms the compared methods in all situations, with the exclusion of the one case that Lalonde's method has 0.01 better precision on Lalonde's dataset. However, unlike Lalonde's and Guo's methods employing a complex classifier to learn several complicated shadow features, our method only requires a simple verification on Canny edges, indicating the effectiveness of the proposed spectrum ratio properties.

4.3. Results on images without shadows

Previous researchers evaluate their methods on images that do contain shadows. However, if a shadow detection algorithm frequently detects object edges as shadow edges, it may cause new problems rather than bringing any advantages for the later

processing stages. Since the shadow features proposed in this paper represent the essential physical properties of shadows, our shadow verification step can be used to verify whether an arbitrary edge is a shadow edge or not. Therefore, our method can be applied on images that do not contain shadows. To this end, we compare the three shadow detection results on images that do not contain shadows. In Fig. 10, we compare the shadow detection results of our method, Lalonde's method, and Guo's method on two representative images containing a significant number of object edges. Our method outperforms the other two methods in classifying the least amount of non-shadow edges as shadow edges. Specifically, our method does not detect any shadow edges in the first image and detects two squares in the second image. The other two methods find different shadow edges in the first image and a significantly large number of squares as shadow edges in the second image.

4.4. Limitations

The extensive comparison shows the effectiveness of our proposed shadow properties and the shadow detection method. However, our method does not work well on images with overexposed regions. Fig. 11 shows two failure cases for our shadow detector. It shows that the failures mainly occur at overexposed regions. This is because overexposure generally increases pixel values in an image. Non-shadow pixels with values above 255 are truncated to 255. This makes K_H , calculated from the dilated regions of the candidate shadow edges, become smaller than its true values. As a result, the shadow edges do not satisfy our three verification criteria, which lead to the false negative failures at these regions. Our method also has limitation on shadows with soft boundaries. As shown in Fig. 12, we test our method on

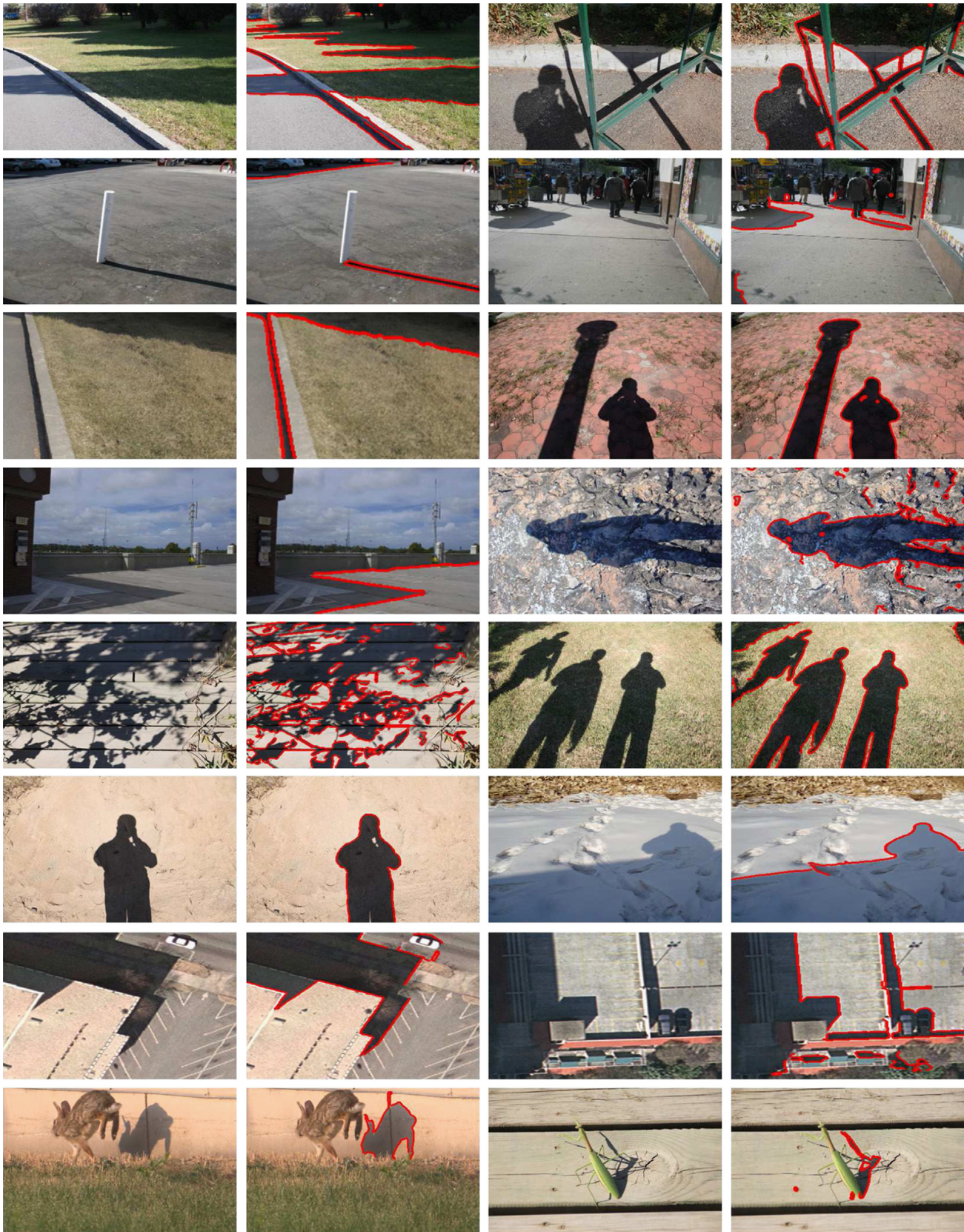


Fig. 9. More results of our shadow detector.

dissolve shadows. We captured dissolve shadows by changing lens with a different focus length. From the results we can find that the detected edges is not continuous when a shadow's boundary

becomes soft. This is mainly because the Canny edge detector cannot extract the boundary out and further lead to the verification step failed in our detection algorithm.

5. Discussion and conclusion

Successfully detecting shadows in still images is challenging yet it has wide applications. New shadow features are apparently important to perform shadow detection and processing. We observe that the ratios of the point-wise product of daylight SPD with sRGB CMFs to the point-wise product of skylight SPD with CMFs roughly approximate a constant (spectrum ratio), despite the dissimilarity between the SPD of daylight and skylight. We also find that the ratios of linear sRGB pixel values of surfaces illuminated by daylight (in non-shadow regions) and skylight (in shadow regions) equal to this constant in each channel. Following this observation, we calculate the ratios under various representative Sun angles. We then find out four physical shadow properties by investigating the common characteristics of the calculated ratios under typical Sun angles.

Based on the discovered four shadow properties, we propose a novel shadow detection algorithm for still images. Our method can effectively extract shadows from a single image with complex outdoor scenes without requiring any prior knowledge. Compared with the state-of-the-art learning-based methods employing a complex classifier to learn several complicated shadow features, our method only requires a simple verification on Canny edges. Such a simple algorithm achieves better shadow detection results in a shorter time, indicating the effectiveness of the proposed

spectrum ratio properties. These advantages may make our algorithm easier to use in practical applications.

Since our shadow detection method contains the verification step, it can work on images without shadows. Furthermore, we may incorporate our shadow edge classification component into other applications. For example, in video surveillance and pattern recognition tasks, the frame difference technique is widely used. However, shadows may also cause changes, e.g., a shadow exists in the background frame but disappears in the current frame. This situation often occurs in practical applications. It may be necessary

Table 4

Comparison of quantitative results in terms of Precision, Recall, and F-measure (P/R/F).

Method	Dataset				All Images
	Tian's	Guo's	Lalonde's	Zhu's	
Lalonde's	0.59/0.72/0.61	0.49/0.69/0.55	0.37/0.63/0.40	0.35/0.66/0.43	0.45/0.68/0.50
Guo's	0.48/0.48/0.40	0.53/0.57/0.51	0.13/0.33/0.17	0.35/0.54/0.36	0.37/0.48/0.36
Ours	0.70/0.78/0.70	0.69/0.73/0.66	0.36/0.66/0.44	0.47/0.67/0.50	0.56/0.70/0.57

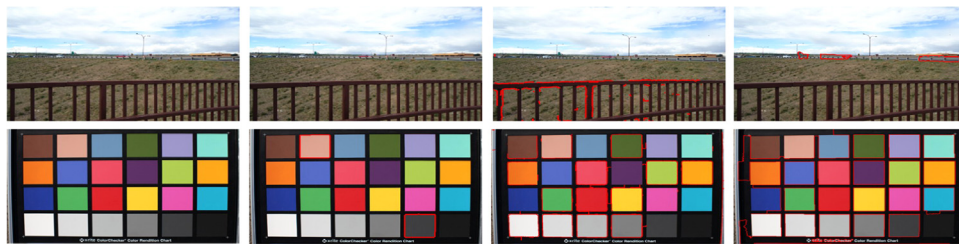


Fig. 10. Comparison of three shadow detection results on two images that do not contain shadows. 1st column: original images; 2nd column: our results; 3rd column: Lalonde's results; 4th column: Guo's results.



Fig. 11. Two failure cases of our shadow detector.



Fig. 12. Detection results on dissolve shadows. Top: original images; bottom: results.

in such a circumstance to perform our shadow edge classification to verify whether the “changes” are caused by shadows.

While extensive comparison validates the advantages of our proposed method, it can fail in some situations due to complicated scenes and illumination, such as overexposure regions, noisy regions, and complex textured regions. One solution is to utilize Sun angle information, which can be easily and accurately determined if the time and the location information are available. For example, in outdoor video surveillance applications, we may have an opportunity to know the time and the location information. As a result, the spectrum ratio properties can be better restricted and our method can be expected to achieve better performance.

Conflict of interest

Non declared.

Acknowledgment

This work was supported by the Natural Science Foundation of China under Grants 61102116 and 61473280.

References

- [1] J.-F. Lalonde, A. Alexei, G. Srinivasa, Estimating natural illumination from a single outdoor image, *IEEE Int. Conf. Comput. Vis.* (2009) 183–190.
- [2] X. Cao, F. Hassan, Camera calibration and light source orientation from solar shadows, *Comput. Vis. Image Underst.* 105 (1) (2007) 60–72.
- [3] H. Kawasaki, R. Furukawa, Shape reconstruction and camera self-calibration using cast shadows and scene geometries, *Int. J. Comput. Vis.* 83 (2) (2009) 135–148.
- [4] G. Finlayson, S. Hordley, C. Lu, M. Drew, On the removal of shadows from images, *IEEE Trans. Pattern Anal. Mach.* 28 (1) (2006) 59–68.
- [5] E. Arbel, H.-O. Hagit, Shadow removal using intensity surfaces and texture anchor points, *IEEE Trans. Pattern Anal. Mach.* 33 (6) (2011) 1202–1216.
- [6] F. Liu, G. Michael, Texture-consistent shadow removal, *Eur. Conf. Comput. Vis.* (2008) 437–450.
- [7] C. Fredembach, G. Finlayson, Hamiltonian path based shadow removal, *Br. Mach. Vis. Conf.* (2005) 502–511.
- [8] N. Martel-Brisson, Z. Andre, Moving cast shadow detection from a Gaussian mixture shadow model, *IEEE Conf. Comput. Vis. Pattern Recognit.* 2 (2) (2005) 643–648.
- [9] S. Nadimi, B. Bir, Physical models for moving shadow and object detection in video, *IEEE Trans. Pattern Anal. Mach.* 26 (8) (2004) 1079–1087.
- [10] C. Benedek, S. Tamcs, Bayesian foreground and shadow detection in uncertain frame rate surveillance videos, *IEEE Trans. Image Process.* 17 (4) (2008) 608–621.
- [11] M.-T. Yang, K.-H. Lo, C.-C. Chiang, W.-K. Tai, Moving cast shadow detection by exploiting multiple cues, *IET Image Process.* 2 (2) (2008) 95–104.
- [12] W. Zhang, X.Z. Fang, X.K. Yang, Q.J. Wu, Moving cast shadows detection using ratio edge, *IEEE Trans. Multimed.* 9 (6) (2007) 1202–1214.
- [13] Y. Wang, K.-F. Loe, J.-K. Wu, A dynamic conditional random field model for foreground and shadow segmentation, *IEEE Trans. Pattern Anal. Mach.* 28 (2) (2006) 279–289.
- [14] J. Björn, W. Johan, F. Per-Erik, G. Gösta, Shadow detection for moving objects based on texture analysis, *Pattern Recognit. Lett.* 30 (8) (2009) 751–759.
- [15] J.-B. Huang, C.-S. Chen, Moving cast shadow detection using physics-based features, *IEEE Conf. Comput. Vis. Pattern Recognit.* (2009) 2310–2317.
- [16] N. Martel-Brisson, A. Zaccarin, Learning and removing cast shadows through a multi distribution approach, *IEEE Trans. Pattern Anal. Mach.* 29 (7) (2007) 1133–1146.
- [17] A.J. Joshi, P. Nikos, Learning to detect moving shadows in dynamic environments, *IEEE Trans. Pattern Anal. Mach.* 30 (11) (2008) 2055–2063.
- [18] A.-N. Nijad, E. Helmut, S. Jyoti, E.A. Eran, A survey of cast shadow detection algorithms, *Pattern Recognit. Lett.* 33 (6) (2012) 752–764.
- [19] A. Sanin, S. Conrad, C.L. Brian, Shadow detection: a survey and comparative evaluation of recent methods, *Pattern Recognit.* 45 (4) (2012) 1684–1695.
- [20] G. Finlayson, F. Clément, M. Drew, Detecting illumination in images, *IEEE Int. Conf. Comput. Vis.* (2007) 1–8.
- [21] H. Iwama, Y. Makihara, Y. Yagi, Foreground and shadow segmentation based on a homography-correspondence pair, *Asian Conf. Comput. Vis.* (2010) 702–715.
- [22] J. Yao, Z. Zhongfei Mark, Hierarchical shadow detection for color aerial images, *Comput. Vis. Image Underst.* 102 (1) (2006) 60–69.
- [23] K.-L. Chung, Y.-R. Lin, Y.-H. Huang, Efficient shadow detection of color aerial images based on successive thresholding scheme, *IEEE Trans. Geosci. Remote Sens.* 47 (2) (2009) 671–682.
- [24] A. Makarau, R. Richter, R. Muller, P. Reinartz, Adaptive shadow detection using a blackbody radiator model, *IEEE Trans. Geosci. Remote Sens.* 49 (6) (2011) 2049–2059.
- [25] J.-F. Lalonde, A.A. Efros, S.G. Narasimhan, Detecting ground shadows in outdoor consumer photographs, *Eur. Conf. Comput. Vis.* (2010) 322–335.
- [26] J. Zhu, K. Samuel, S.Z. Masood, Learning to recognize shadows in monochromatic natural images, *IEEE Conf. Comput. Vis. Pattern Recognit.* (2010) 223–230.
- [27] R. Guo, D. Qieyun, H. Derek, Paired regions for shadow detection and removal, *IEEE Trans. Pattern Anal. Mach.* 35 (12) (2013) 2956–2967.
- [28] A. Panagopoulos, S. Dimitris, P. Nikos, Robust shadow and illumination estimation using a mixture model, *IEEE Conf. Comput. Vis. Pattern Recognit.* (2009) 651–658.
- [29] F. Graham, H. Steven, S. Gerald, G.Y. Tian, Illuminant and device invariant colour using histogram equalization, *Pattern Recognit.* 38 (2) (2005) 179–190.
- [30] A. Leone, D. Cosimo, Shadow detection for moving objects based on texture analysis, *Pattern Recognit.* 40 (4) (2007) 1222–1233.
- [31] B.A. Maxwell, R.M. Friedhoff, C.A. Smith, A bi-illuminant dichromatic reflection model for understanding images, *IEEE Conf. Comput. Vis. Pattern Recognit.* (2008) 1–8.
- [32] R. Ramamoorthi, M. Dhruv, B. Peter, A first-order analysis of lighting, shading, and shadows, *ACM Trans. Graph.* 26 (1) (2007) 1–21.
- [33] J.D. Tian, J. Sun, Y.D. Tang, Tricolor attenuation model for shadow detection, *IEEE Trans. Image Process.* 18 (10) (2009) 2355–2363.
- [34] J.D. Tian, Y.D. Tang, Linearity of each channel pixel values from a surface in and out of shadows and its applications, *IEEE Conf. Comput. Vis. Pattern Recognit.* (2011) 985–992.
- [35] ASTM-E308-01, Standard practice for computing the colors of objects by using the CIE system, *ASTM Int.* (2001) 9–10.
- [36] C. Gueymard, SMARTS2: a simple model of the atmospheric radiative transfer of sunshine: algorithms and performance assessment, in: Florida Solar Energy Center Cocoa, FL, 1995.
- [37] A. Berk, L.S. Bernstein, D.C. Robertson, Modtran: a moderate resolution model for lowtran, Technical Report, DTIC Document, 1987.
- [38] D. Hoiem, A.E. Alexei, H. Martial, Recovering surface layout from an image, *Int. J. Comput. Vis.* 75 (1) (2007) 151–172.

Jiandong Tian received his B.S. Tech. degree in Automation at Heilongjiang University, PR China, in 2005. He received his Ph.D. degree in Pattern Recognition and Intelligent System at Chinese Academy of Sciences, PR China, in 2011. He is currently an Associate Professor in Computer Vision at State Key Laboratory of Robotic, Shenyang Institute of Automation, Chinese Academy of Sciences. His research interests include pattern recognition and robot vision.

Xiaojuan Qi received the B.S. degree in Computer Science from Donghua University, Shanghai, China, in 1993, the M.S. degree in Pattern Recognition and Intelligent System from Shenyang Institute of Automation, the Chinese Academy of Sciences, Shenyang, China, in 1996, and the Ph.D. degree in Computer Science from Louisiana State University, Baton Rouge, USA, in 2001. In Fall 2002, she joined the Department of Computer Science at Utah State University as tenure-track Assistant Professor. In April 2008, she received tenure and was promoted to Associate Professor. Her research interests include content-based image retrieval, digital image watermarking, pattern recognition, and computer vision.

Liangqiong Qu received the B.S. degree in Automation from Central South University, China, in 2011. She is currently pursuing the Ph.D. degree in Pattern Recognition and Intelligent Systems at the State Key Laboratory of Robotics, Shenyang Institute of Automation, Chinese Academy of Sciences. As a Joint-Ph.D. student, she is now studying at the City University of Hong Kong, Hong Kong (from September 2014 to February 2016). Her research interests include illumination modeling and image processing.

Yandong Tang received B.S. and M.S. degrees in the Department of Mathematics, Shandong University, in 1984 and 1987, respectively. In 2002 he received the Doctor's degree in Applied Mathematics from the University of Bremen, Germany. Currently he is a Professor in Shenyang Institute of Automation, Chinese Academy of Sciences. His research interests include robot vision, pattern recognition and numerical computation.